

Coregistered photoacoustic and ultrasound imaging and classification of ovarian cancer: *ex vivo* and *in vivo* studies

Hassan S. Salehi
Hai Li
Alex Merkulov
Patrick D. Kumavor
Hamed Vavadi
Melinda Sanders
Angela Kueck
Molly A. Brewer
Quing Zhu

Coregistered photoacoustic and ultrasound imaging and classification of ovarian cancer: *ex vivo* and *in vivo* studies

Hassan S. Salehi,^{a,†} Hai Li,^{a,†} Alex Merkulov,^b Patrick D. Kumavor,^c Hamed Vavadi,^c Melinda Sanders,^d Angela Kueck,^e Molly A. Brewer,^e and Quing Zhu^{a,c,*}

^aUniversity of Connecticut, Department of Electrical and Computer Engineering, Storrs, Connecticut 06269, United States

^bUniversity of Connecticut Health Center, Division of Radiology, Farmington, Connecticut 06030, United States

^cUniversity of Connecticut, Department of Biomedical Engineering, Storrs, Connecticut 06269, United States

^dUniversity of Connecticut Health Center, Department of Pathology, Farmington, Connecticut 06030, United States

^eUniversity of Connecticut Health Center, Division of Gynecologic Oncology, Farmington, Connecticut 06030, United States

Abstract. Most ovarian cancers are diagnosed at advanced stages due to the lack of efficacious screening techniques. Photoacoustic tomography (PAT) has a potential to image tumor angiogenesis and detect early neovascular changes of the ovary. We have developed a coregistered PAT and ultrasound (US) prototype system for real-time assessment of ovarian masses. Features extracted from PAT and US angular beams, envelopes, and images were input to a logistic classifier and a support vector machine (SVM) classifier to diagnose ovaries as benign or malignant. A total of 25 excised ovaries of 15 patients were studied and the logistic and SVM classifiers achieved sensitivities of 70.4 and 87.7%, and specificities of 95.6 and 97.9%, respectively. Furthermore, the ovaries of two patients were noninvasively imaged using the PAT/US system before surgical excision. By using five significant features and the logistic classifier, 12 out of 14 images (86% sensitivity) from a malignant ovarian mass and all 17 images (100% specificity) from a benign mass were accurately classified; the SVM correctly classified 10 out of 14 malignant images (71% sensitivity) and all 17 benign images (100% specificity). These initial results demonstrate the clinical potential of the PAT/US technique for ovarian cancer diagnosis. © 2016 Society of Photo-Optical Instrumentation Engineers (SPIE) [DOI: 10.1117/1.JBO.21.4.046006]

Keywords: imaging systems; medical optics and biotechnology; photoacoustic imaging; ultrasound; classification algorithms; clinical applications.

Paper 150521RR received Aug. 5, 2015; accepted for publication Mar. 24, 2016; published online Apr. 18, 2016.

1 Introduction

Ovarian cancer ranks fifth as the cause of cancer deaths in women. Due to nonspecific associated symptoms as well as lack of efficacious screening techniques at the disposal of patients, the survival rate for ovarian cancer has not significantly improved over the last two decades. Therefore, ovarian cancer has the highest mortality rate of all the gynecologic cancers with a five-year survival rate of ~33% when the disease is diagnosed at later stages.¹⁻³ Bilateral risk-reducing salpingo-oophorectomy (RRSO) is widely used for cancer risk reduction in women with BRCA1 and BRCA2 (BRCA1/2) mutations.⁴ Although RRSO significantly reduces breast cancer risk by ~50% and ovarian cancer risk by 80 to 95%,⁵ it may be accompanied by menopausal symptoms, impaired quality of life, and increased cardiovascular risk.⁶ Screening asymptomatic women for ovarian cancer does not reduce mortality nor improve diagnosis at an advanced stage, and it is often associated with unnecessary surgery.⁷ Transvaginal ultrasound (US) has been useful to assess ovarian volume, which may be associated with greater ovarian cancer risk, but it may only be detectable once the ovary has enlarged and cancer often has already metastasized.⁸ As a result, there is an urgent need to improve the current clinical practice by advancing transvaginal US and detecting early malignancies in the ovary.

Photoacoustic tomography (PAT) is an emerging imaging modality that images optical absorption contrast in tissue based on ultrasonic detection through the photoacoustic effect.⁹⁻¹² To obtain the PAT images, biological tissue is illuminated with short laser pulses. Laser energy absorbed by the tissue produces transient thermoelastic expansion and generates wideband acoustic waves, which are detected by a US transducer for reconstruction of the optical absorption distribution of the tissue.¹³⁻¹⁵ Optical absorption distributions at multiple wavelengths can be used to map tumor hemoglobin distribution and oxygen saturation; this is clinically important because abnormal vascularization and lower blood oxygenation in tumors may indicate the presence of cancer.

We have developed a coregistered photoacoustic and ultrasound (PAT/US) system and imaging probe for noninvasive transvaginal imaging of human ovaries,¹⁶⁻¹⁹ and photoacoustic feature-based classification algorithms for differentiating malignant from benign *ex vivo* ovarian tissues.^{20,21} To overcome the challenges of light delivery and photoacoustic/ultrasound data acquisition speed for patient studies, our coregistered PAT/US imaging system has made significant advances. This is from the initial free space light delivery and slow data acquisition,¹⁴ to fiber assembly based light delivery and real-time data acquisition of 64 channels,¹⁶ and finally to its present miniaturized and optimal fiber-based light delivery^{18,19} and real-time data acquisition of 128 channels.¹⁷ Furthermore, to accurately and

*Address all correspondence to: Quing Zhu, E-mail: zhu@engr.uconn.edu

[†]These authors contributed equally to this work.

robustly characterize malignant from benign ovarian tissues, our feature extraction and classifiers have evolved from single threshold-based classifiers¹⁴ to image feature-based classifiers,²⁰ and to image and spectra features based classifiers.²¹ In this study, we report results from a new set of 25 excised ovaries of 15 patients, and two patients studied both *in vivo* and *ex vivo* with malignant and benign pathology using our upgraded coregistered real-time PAT/US clinical prototype system¹⁷ with optimized light delivery and improved signal-to-noise ratio.^{18,19} In addition to features obtained from the PAT data, we extracted six new features with three of them from the US beam spectra, to improve the diagnostic performance of the logistic and support vector machine (SVM) classifiers. We then implemented a forward sequential feature (FSF) selection method to select five significant features from an initial 23 features obtained from the *ex vivo* data and applied these five features for diagnosis of ovarian masses in the *in vivo* studies of two patients (one malignant case and one benign case). To the best of our knowledge, this study is the first one reporting quantitative analysis of *in vivo* PAT/US imaging to classify malignant and benign human ovarian masses. Quantitative analysis of *in vivo* PAT/US imaging could potentially be used as a noninvasive screening tool in assisting physicians to characterize and diagnose benign and malignant ovarian tissues.

2 Methods and Materials

2.1 Photoacoustic and Ultrasound Imaging System

The transvaginal coregistered PAT/US imaging system used in the clinical study is shown in Fig. 1. The details of the light delivery subsystem and real-time PAT/US subsystem can be found in our earlier publications.^{17–19} Briefly, the PAT/US imaging system consisted of a laser source, a fiber-optic light delivery system, a transvaginal US probe, and a real-time PAT/US data acquisition and processing module. The laser light propagates through a single homemade lens array that consisted of four cylindrical lenses (Edmund Optics Inc., Barrington, New Jersey). The lenses were arranged such that two were in front and the other two behind and orthogonally positioned (rotated 90 deg) to the pair in front. With the incident laser light centered on the lens array, the latter split and focused the beam into four separate and equal spots.¹⁹ Each beam was coupled into a 1 mm core optical fiber with a numerical aperture of 0.48. The distal ends of the illumination fibers were affixed to the compact

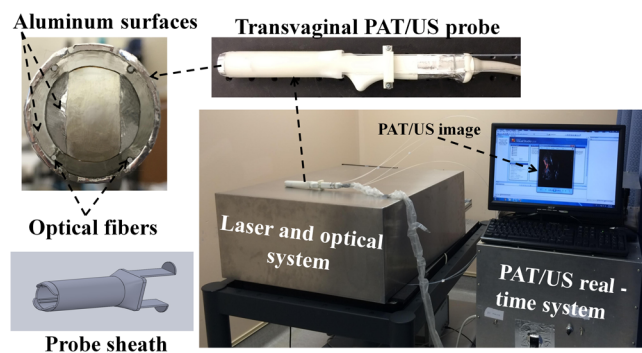


Fig. 1 The transvaginal coregistered photoacoustic/ultrasound imaging system located at the Radiology Department of the UCONN Health Center for patients' studies.

PAT/US imaging probe. The probe consists of a 128-element transvaginal US array of 6 MHz central frequency and 80% bandwidth (W.L. Gore and Associates, Inc., Newark, Delaware), integrated with a custom-made sheath with a 25 mm outer diameter. The radius of the US probe is 8 mm and elements are evenly spread over 2.56 rad. The sheath encases both the transducer and fibers. In the clinical studies, the probe was covered by a transparent condom, which is typically used in transvaginal US examination of the ovaries. The laser source is a tunable Ti:sapphire laser (LS-2211, Symphotics TII, Camarillo, California) pumped by a Q-switched Nd:YAG laser (LS-2134, Symphotics TII) and delivers 20 ns pulses at 15 Hz repetition rate. The laser fluence on the tissue surface was ~ 20 mJ/cm² at 750 nm wavelength, and is below the American National Standards Institute safety limit (25 mJ/cm²).²² During *in vivo* imaging, ovaries were imaged using four preselected wavelengths of 720, 750, 790, and 830 nm with a total tuning time of ~ 20 s for these four wavelengths. For *ex vivo* studies, the wavelength was fixed at 750 nm. The data acquisition of the imaging system provided up to 15 coregistered image frames per second, with the speed limited by the laser pulse repetition rate. In the coregistered mode, the US and PAT modules ran in a time division multiplexing approach; the PAT module was synchronized with the laser pulses and the US module ran in the periods between the pulses (when no pulses were present).¹⁷ The US transmission focus was fixed to 25 mm in all the experiments.

2.2 Human Subjects

This group of human ovaries was obtained from 16 patients (age: 39 to 70 years; average: 55 years) who underwent prophylactic oophorectomy (PO) from March 2014 to January 2015 at the University of Connecticut Health Center (UCHC), and imaged *ex vivo* using the transvaginal system shown in Fig. 1. These patients were either at risk for ovarian cancer or they had ovarian mass or pelvic mass suggesting malignancy. One patient's ovaries were excluded from analysis because blue dye was present on both ovaries and caused significant imaging artifacts. The *ex vivo* imaging was performed by sequentially scanning the ovary using a mechanical stage controlled manually. Five to ten independent image frames were obtained from each ovary depending on the size of the specimen. The ovary was mounted on a supporting frame made of a transparent thin optical fiber and immersed at a depth of ~ 10 mm from the probe surface in a tank filled with calibrated intralipid solution with an absorption coefficient of 0.02 cm⁻¹ and reduced scattering coefficient of 4 cm⁻¹. These optical properties were estimated from measurements of porcine vagina muscle walls. Additionally, two patients who had suspicious ovarian masses were imaged *in vivo* four to eight days before PO using the hand-held transvaginal probe at the four preselected wavelengths. Scanning was performed at multiple independent locations by an attending US technologist. In addition, *ex vivo* PAT/US data were obtained from the same ovaries after PO. The ovary side facing the vagina was identified during the surgery by the surgeon using a suture. This way, the comparison of the *in vivo* and *ex vivo* images was made feasible. Table 1 provides patient information and diagnosis of the ovaries.

This study was approved by the institutional review board of UCHC, and informed consent was obtained from all patients. For the *ex vivo* studies, the excised ovaries were kept in a 0.9% wt/vol NaCl solution and imaged within a few hours after

Table 1 Patient information and ovary diagnosis for classification.

Patient #	Ovary #	Age	Menopausal status	Histology	Diagnosis
1	1a	69	Post	High-grade, serous epithelial carcinoma	Malignant
	1b				Benign
2	2a	40	Pre	Few follicles, blood vessels, simple cyst, corpus luteum	Benign
	2b				Benign
3 ^a	3a	56	Pre	Endometriosis (calcium, iron), scar, fibrosis, some blood vessels, dense stroma	Benign
4	4a	53	Post	Low-grade endometrioid, necrosis	Malignant
5	5a	52	Pre	Calcium, iron, blood vessels	Benign
	5b				Benign
6	6a	58	Post	Simple cyst, surface bumps	Benign
	6b				Benign
7	7a	39	Pre	Endometriosis	Benign
8	8a	59	Post	Corpora albicans, blood vessels, dense stroma	Benign
	8b				Benign
9	9a	68	Post	Stromal predominance, high-grade, serous epithelial carcinoma	Benign
	9b				Malignant
10	10a	55	Pre	Corpora albicans, dense stroma	Benign
	10b				Benign
11	11a	43	Pre	Dilated follicles, corpora albicans, dense stroma, less collagen, hemorrhage, corpus luteum	Benign
	11b				Benign
12	12a	55	Pre	Corpora albicans, scars, calcification of surface, big cystic space, hemorrhage, corpus luteum	Benign
	12b				Benign
13	13a	39	Pre	Inclusion cyst, calcification	Benign
	13b				Benign
14	14a	70	Post	Blood vessels, calcification	Benign
15 ^a	15a	62	Post	High grade, surface serous epithelial carcinoma	Malignant

^aIn both *in vivo* and *ex vivo* studies.

oophorectomy. After the PAT/US imaging, the ovaries were fixed in 10% formalin solution and returned to the Pathology Department for histological processing. For the histologic evaluation, the ovaries were cut into 5 mm blocks parallel to the imaging plane, dehydrated with graded alcohol, embedded in paraffin, and sectioned into 7 μ m thicknesses using a paraffin microtome. The hematoxylin and eosin (H&E) slides were used to compare with PAT/US imaging findings.

2.3 Feature Extraction

The conventional delay-and-sum beamforming algorithm was used for both the PAT and US image formation. Each angular

PAT and US beam was formed by summation of the delayed radio frequency signals from the nearest 65 channels with respect to the beam direction. The PAT and US beam envelopes were obtained by base-band demodulation and amplitude detection. PAT and US images were constructed by a linear mapping of envelopes after scan conversion.²¹ We paid special attention to selecting visually different images in the image sequence of each ovary to provide more independent data to classifiers. Similar to our earlier study, 17 features were initially extracted from the PAT data for classification of malignant and benign ovarian tissues; these features include two out of three PAT beam spectral features, five PAT beam envelope features, and ten PAT imaging features.²¹

Briefly, spectral features (spectral slopes, mid-band fits, and 0 MHz intercepts) from PAT beams reveal the distribution of the frequency components within the frequency range of the transducer array, and are related to absorber dimensions and chromophore concentrations.^{21,23,24} Features from the PAT beam envelopes, such as the summation of envelopes (PAT summation) and the maximum envelope, characterize the light fluence and absorption within the selected suspicious area or region of interest (ROI). The ROI was selected by first estimating the center (x_0 and y_0) using a Gaussian model fitted to 0 and 90 deg Radon transforms of a PAT image along the x - and y -axes, respectively.^{20,21} The Gaussian model is given as

$$f(x) = \exp\left[-\frac{(x - \mu)^2}{2\sigma^2}\right],$$

where μ is the index of the estimated center and σ is the standard deviation representing the spatial spread of vasculature along the projection direction. Using the estimated center, a 1.5 cm by 1.5 cm square image was cropped and used to extract image related features. The annular beams within the ROI were selected for feature extraction of the beams. The spectrum of each beam was obtained by Fourier transform and then calibrated to the transducer frequency response measured at an elevation focus depth of 2.5 cm. The average center depth of ROIs of all imaging frames was 2.13 cm (± 0.25 cm), which was very close to the transmission focus depth of 2.5 cm. Since the PAT and US beam spectra were calculated within a narrow ~ 1.5 cm beam segment around the center of the ROI, the depth-dependent transducer response had minor effect and was not accounted for. The average beam spectral features were then used as corresponding features of image frames. PAT summation was the total summation of envelopes higher than the system noise threshold within the selected ROI. The system noise was estimated from the mean envelope peaks of regions further away from the transducer where almost no photoacoustic signal was generated.²¹ PAT area is the number of pixels with envelopes larger than system noise threshold in the ROI. PAT beam envelope homogeneity is defined as the mean value of the correlation of two consecutive PAT beam segments in the ROI and characterizes the spatial heterogeneity of the PAT images. Statistical analysis was performed on the PAT images to obtain mean values and variances of the normalized pixel values. From our experimental observations, the PAT images of malignant cases usually showed clustered distributions due to the abundance of localized smaller vessels, whereas the distribution was more diffused, scattered, and spatially spread out in the normal cases.^{20,21} The normalized Radon transforms from 0 to 90 deg with an interval of 1 deg were calculated and fed to the Gaussian model after averaging. The fitting error is defined as the norm of the difference between the mean Radon transform and the fitted value from the Gaussian model. For a benign case, its PAT image tends to be more uniform, which results in a closer match to the Gaussian model. For a malignant case, its PAT image is heterogeneous, which produces a larger difference from the Gaussian model. The standard deviation of the Gaussian model was used as a feature to describe the overall spatial spread of the photoacoustic intensity.

Linear and nonlinear composite spatial filters developed in Refs. 25 and 26 were constructed to maximize the ratio of output peak to output energy. They acted as a template for malignant ovarian tissues and a template for benign tissues when the

construction was applied on training PAT images obtained from malignant ovaries and PAT images from benign ovaries, respectively. The spatial filter constructed from the PAT images of malignant ovaries served as an image template for malignant ovarian tissues (malignant filter). The common spatial frequency features of malignant ovaries, which were not visibly distinguishable, were embedded in this template. The peak output of this spatial filter was the maximum value of the correlation of the input image with this malignant ovary template. A high output from this filter meant a high similarity to malignant ovary and a low output was expected for benign ovaries. (see the Appendix for more details).

Additionally, we included new US spectral features in this study. The US spectrum analysis developed by Lizzi and coworkers^{27,28} showed that US pulse-echo spectral parameters were related to the lesion attenuation, sizes, concentrations, and relative acoustic impedances of scatterers. These features have shown promise in cancer detection and classification of the eye,²⁸ prostate,²⁹ and breast.³⁰ We expect these features to be useful additions to improve PAT feature-based classification of malignant and benign ovarian tissues. Three features were extracted from the US beams after calibration with the transducer frequency response for spectral analysis; they are US spectral slope, US 0 MHz intercept, and US mid-band fit. Every US beam segment in the ROI was multiplied by a Hamming window before spectral feature extraction. The averaged value of each spectral feature was used to characterize each imaging frame. In addition, we extracted the ovary area from US images by modeling the ovary as an ellipsoid and measuring its lengths of long and short axes. In the *ex vivo* data, malignant ovaries had a larger average size than that of benign ones. Furthermore, the mean value of PAT envelop was also extracted in addition to existing maximum PAT envelope and PAT summation features, and found to be valuable in the *ex vivo* data classification. We also included the menopausal status of patients in our extracted features for classifier input (1 represents postmenopausal, 0 represents premenopausal).

In comparison to our earlier studies, the light delivery setup of our PAT/US system was optimized^{18,19} and the data acquisition system was upgraded from 64 channels to 128 channels,¹⁷ thus providing improved signal-to-noise ratio. In addition to the 17 PAT features,²¹ six new features from the US spectrum, mean PAT envelop, ovary area, and patient menopausal status were included to improve the ovarian tissue characterization. Therefore, a total of 23 features were initially extracted.

2.4 Logistic Model and Support Vector Machine Classifiers

Logistic regression is widely used in medical studies.^{31,32} Logistic regression belongs to the class of generalized linear model based on the exponential distribution family. It is a statistical model that can describe the relationship between several predictor variables X_1, X_2, \dots, X_k and a dichotomous response variable Y (0 or 1). The probability of occurrence of one of the two possible outcomes of Y can be described by the following equation:³³

$$P(Y = 1 | X_1, X_2, \dots, X_k) = \left\{ 1 + \exp\left[-\left(\beta_0 + \sum_{n=1}^k \beta_n x_n\right)\right] \right\}^{-1},$$

where β_0 is a constant term and β_n is the coefficient for each feature X_k . The constant term and coefficients can be estimated from the training group data using maximum likelihood estimation and then used on the testing group for validation. In this study, the logistic model was utilized to classify benign and malignant ovarian tissues. The features extracted from the PAT and US data were used as predictor variables, and the actual diagnosis results were used as the response in training (1 represents malignant and 0 represents benign). In the testing set, a threshold of 0.5 was used to obtain the sensitivity, specificity, positive predictive, and negative predictive values (PPV, NPV). By varying the threshold, the receiver operating characteristic (ROC) curve can be derived and the area under ROC curve (AUC) can be calculated to demonstrate the performance of this logistic classifier.

The SVM optimizes the separation of two populations of data by using a linear or nonlinear kernel. It maps the input data into high-dimensional feature spaces and finds the hyperplane that leads to the best discrimination between the two populations.³⁴ The SVM package in MATLAB[®] was used with a radial basis function (RBF) kernel, where the sequential minimal optimization method was used to find a hyperplane threshold that separates the malignant from benign cases. SVM with a polynomial kernel was also investigated; however, the testing results were not as good as those of RBF kernel. Therefore, SVM with RBF kernel was used in our data analysis. The training was terminated when 100% sensitivity and specificity were achieved or when high iterations (1000) had been reached. The trained SVM structure was then applied to the testing samples for validation.

Table 2 Mean features of *ex vivo* ovaries and their order after FSF selection. Underscored features are the optimal features used for *in vivo* classification.

Category	Feature index and name	Mean value (malignant $n = 56$)	Mean value (benign $n = 145$)	p value	FSF index
Spectral features	1. PAT spectral slope (dB/MHz)	-1.50 ± 0.38	-2.14 ± 0.51	0.006	1
	2. US spectral slope (dB/MHz)	-0.27 ± 0.17	-0.42 ± 0.38	<0.001	13
	3. PAT 0 MHz intercept (dB)	-1.30 ± 4.79	-1.84 ± 3.37	<0.001	10
	4. US mid-band fit (dB)	-12.52 ± 6.84	-8.45 ± 2.13	<0.001	5
	5. Maximum PAT envelope	512.81 ± 211.21	361.72 ± 194.77	0.011	6
PAT envelope	6. Mean PAT envelope	263 ± 92	155 ± 48	<0.001	7
	7. PAT summation	$1.35E7 \pm 2.09E6$	$6.52E6 \pm 5.92E5$	0.017	3
	8. PAT envelope homogeneity	0.51 ± 0.09	0.65 ± 0.11	<0.001	2
	9. PAT area (pixel)	442 ± 140	352 ± 214	<0.001	14
PAT image	10. Mean PAT pixel	56.38 ± 6.15	48.97 ± 6.77	<0.001	15
	11. Gaussian fitting error	2.91 ± 2.08	1.87 ± 1.42	0.005	11
	12. Max malignant spatial filter output (malignant, $k = 0.01$)	0.56 ± 0.12	0.43 ± 0.08	<0.001	8
	13. Max benign spatial filter output (benign, $k = 1/3$)	5.48 ± 0.79	6.66 ± 2.01	<0.001	12
Others	14. Ovary area (mm ²)	781.95 ± 393.47	351.03 ± 285.01	<0.001	9
	15. Menopausal (1: post, 0: pre)			<0.001	4
	16. US 0 MHz intercept	-1.28 ± 2.62	-1.32 ± 2.44	>0.05	n/a
Features with p value >0.05	17. Scale parameter of Rayleigh fitting of envelopes	131.79 ± 22.26	126.13 ± 39.98	>0.05	n/a
	18. PAT variance	2456.9 ± 734.29	2198.2 ± 681.41	>0.05	n/a
	19. Spatial spread of suspicious area	8.45 ± 2.89	9.04 ± 3.28	>0.05	n/a
	20. Max malignant spatial filter output (malignant, $k = 1$)	512.30 ± 268.11	497.18 ± 269.89	>0.05	n/a
	21. Max malignant spatial filter output (malignant, $k = 1/3$)	4.78 ± 1.86	4.94 ± 1.69	>0.05	n/a
	22. Max benign spatial filter output (benign, $k = 1$)	556.87 ± 188.43	530.75 ± 193.44	>0.05	n/a
	23. Max benign spatial filter output (benign, $k = 0.01$)	0.693 ± 0.186	0.716 ± 0.204	>0.05	n/a

Note: n/a, not available

3 Results

3.1 Features Selected from Ex Vivo Data

For a total of 23 initial features, there were $2^{23} - 1$ choices of feature combinations for final classification because each feature can be included or excluded. The null set (no feature is included for classification) cannot be selected. However, it is computationally intensive to evaluate every one of them for obtaining the optimal subset. Instead, we applied a feature selection method to obtain a suboptimal set. Previously, we simply ranked features according to the decreasing order of p values from Student's t test of each feature. In this study, we first excluded eight features with p value >0.05 and selected 15 features for classification as shown in Table 2. The 15 selected features were further ranked by the forward sequential feature (FSF) selection method.³⁵ The criterion used in the FSF method is the misclassification error (the ratio of the number of misclassified images over the total number of images) of the testing group as shown in Fig. 2. Initially, the selected feature group was empty with all 15 features unselected. We then used each single feature for the classifiers and used the misclassification error of the testing group as the criterion. The feature that generated a minimal misclassification error was placed into the selected group. After that, we chose the second feature from the remaining 14 unselected features whose combination with the selected feature (the first one) gave the minimal misclassification error. This procedure was repeated until all features were selected. In this way, the feature order generated from the FSF could present the estimated optimal subsets for classification performance evaluation. As shown in Fig. 2, when the first nine features in the order generated from the FSF method were used, both classifiers achieved their minimal misclassification error. Therefore, these nine features were selected as optimal features for both classifiers. Note that p values were obtained from images of all patients. $p = 0.05$ is a typical value to exclude statistically nonsignificant features. The FSF index was sorted based on the misclassification error for the testing group. Therefore, there was no exact mapping where smaller p values correspond to lower FSF indices.

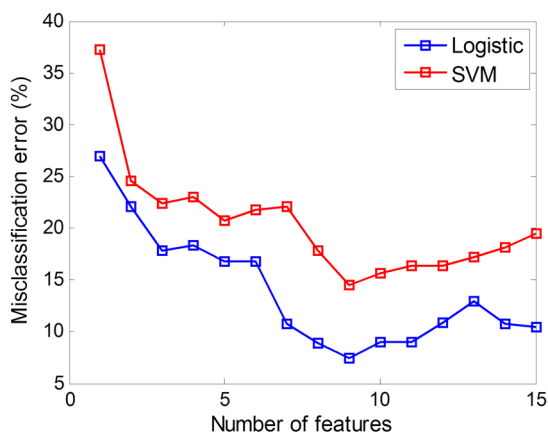


Fig. 2 Misclassification error of both classifiers with respect to different numbers of features in the order from the FSF method. Both classifiers achieved minimal misclassification error when first nine features were used.

3.2 Features Selected Based on Ex Vivo Data for In Vivo Application

We used the *ex vivo* studies to determine suitable features for classification of the *in vivo* data. For the *in vivo* data, PAT summation, and the max and mean PAT beam envelope were found to be not useful as features. This was because the light fluence on the ovarian tissue surface in the *ex vivo* and *in vivo* imaging conditions was different due to the presence of vagina muscle wall in the *in vivo* study. Additionally, we found the ovary size was not an important feature based on the limited *in vivo* data. The final five features selected for *in vivo* classification were PAT spectral slope (dB/MHz, FSF index #1), US mid-band fit (dB) (FSF index #5), PAT beam envelope homogeneity (FSF index #2), max malignant spatial filter output (FSF index #8), and patient menopausal status (FSF index #4). As shown in Fig. 3, the absolute value of the fitted slope of the malignant sample [Fig. 3(d)] is smaller than that of the benign one [Fig. 3(c)], indicating more high-frequency components in its beams, while the absolute value of US mid-band fit in the malignant case [Fig. 3(f)] is larger than the benign case [Fig. 3(e)].

There were in total 201 imaging frames (145 benign and 56 malignant) obtained from the 25 *ex vivo* ovaries of 15 patients. We then equally and randomly partitioned the data pool into two groups, one group for training and another group for testing. This data processing procedure was repeated 50 times to obtain the average performance of classifiers. The *ex vivo* data of the two patients imaged *in vivo* were always kept in the testing group to avoid their influence on *in vivo* diagnosis. The trained structures of the logistic and SVM classifiers were used for both *ex vivo* and *in vivo* data classification.

3.3 In Vivo Example

An example of coregistered PAT/US image of an enlarged ovarian mass of a 62-year-old postmenopausal patient acquired *in vivo* is presented in Fig. 4(a). The PAT images reveal a high-level vascularity on the surface of the ovary from multiple images acquired at multiple positions. After oophorectomy, the same ovary was imaged *ex vivo* and is shown in Fig. 4(b). In the US images, a complex mixed solid and cystic ovarian mass is clearly shown as a homogeneous low echogenic pattern in both *in vivo* and *ex vivo* images. Figure 4(c) is the photograph of the excised ovary with lines marking the PAT/US two-dimensional (2-D) scanning positions. The surgical pathology reported ~65% pink-tan, rubbery tissue and 35% cystic structure with early stage carcinoma (T1c) on the ovary surface. This was an accidental finding because of the enlarged ovarian mass seen by the x-ray computed tomography (CT) and transvaginal US. The H&E slides from the marked region showed high-grade serous epithelial carcinoma on the ovary surface. Figure 4(e) highlights the microvessels as pointed to by the arrows. This example demonstrates the clinical potential of coregistered PAT/US in identifying surface abnormal vascularity of a postmenopausal ovary.

3.4 Statistics of Ex Vivo and In Vivo Results

Figure 5 shows boxplots and p values of five selected features of benign and malignant *ex vivo* ovary groups. To provide readers with a statistical performance of these parameters, data from both training and testing sets were used in these plots. The

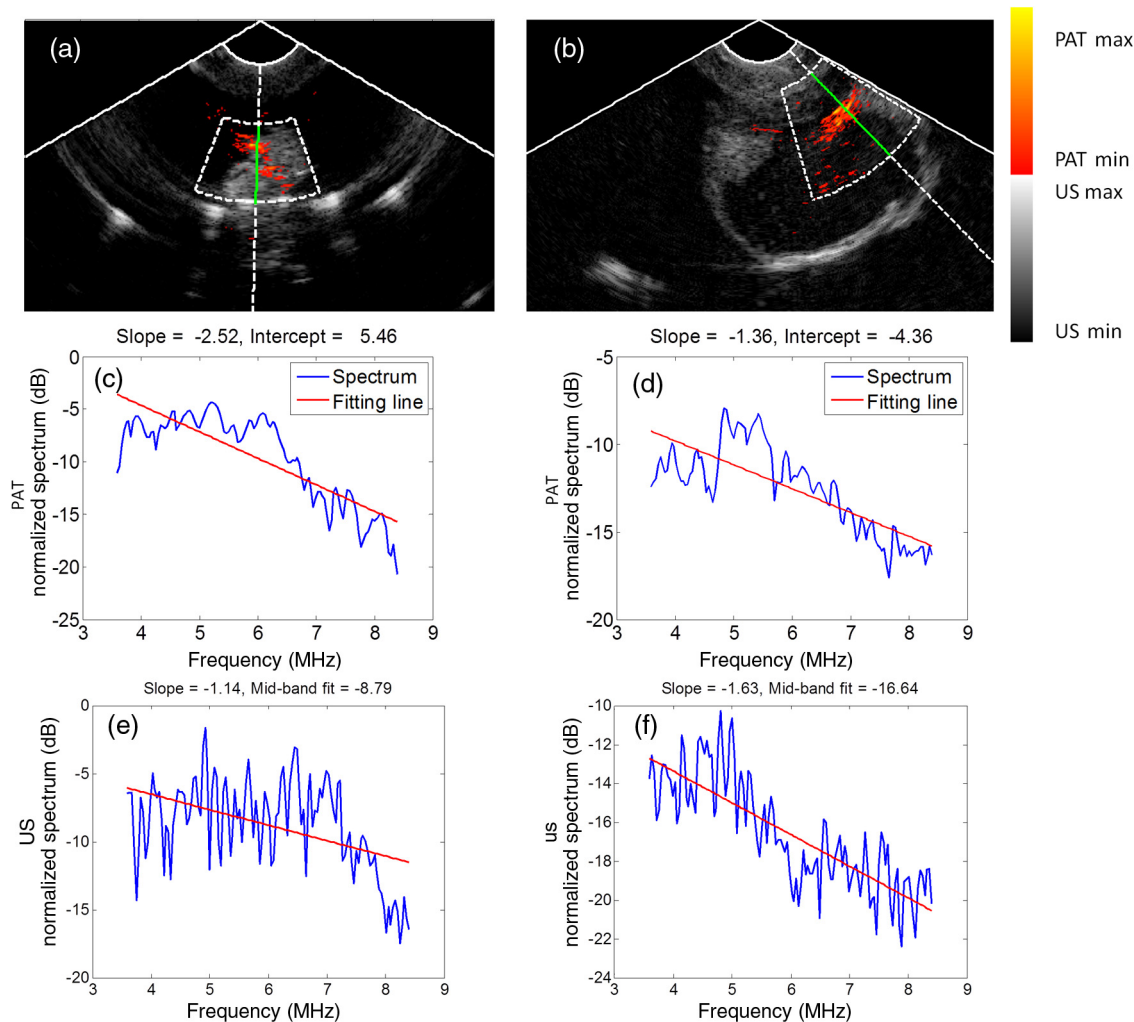


Fig. 3 (a) *Ex vivo* coregistered PAT/US image of a premenopausal benign ovarian tissue and (b) *ex vivo* coregistered PAT/US image of a postmenopausal malignant ovarian tissue. In (a) and (b), the annular fan shapes define the region of beam spectrum feature extraction. (c) The spectrum (blue) and linear fitting (red) of PAT beam of the benign ovarian tissue, (d) the spectrum and linear fitting of PAT beam of the malignant ovarian tissue, (e) the spectrum (blue) and linear fitting (red) of US beam of benign ovary, and (f) the spectrum and linear fitting of US beam of malignant ovarian tissue.

differences were highly statistically significant between benign and malignant groups. These five features were used as predictor variables for the logistic model and SVM to classify benign and malignant ovaries. Figure 6 shows the ROC curve for one set of testing data of the logistic classifier with an AUC of 93.1%.

For the training set, the logistic classifier could achieve a sensitivity of 85.6%, specificity of 87%, PPV of 87%, and NPV of 85.8%. The SVM classifier could achieve over 98% sensitivity, specificity, PPV, and NPV as shown in Table 3(a). For the testing set, the logistic and SVM classifiers could achieve a sensitivity of 70.4 and 87.7%, specificity of 95.6 and 97.9%, PPV of 86.6 and 94.4%, and NPV of 89.4 and 95.4%, respectively.

To evaluate the diagnostic potential of PAT/US features in classifying high-grade serous epithelial carcinoma, the most common type of ovarian cancer, we excluded the image frames of patient #4 who had low-grade endometriosis carcinoma from the data analysis. The diagnostic performance of the classifiers is shown in Table 3(b). It is interesting to note that the sensitivity of both classifiers improved for the testing data; the logistic classifier in particular improved significantly. This finding is

encouraging and suggests that both classifiers may perform better by identifying aggressive high-grade ovarian cancers, which have significantly different surface vasculature and spectral information than the low-grade carcinomas and benign ovarian tissues. This initial result will need to be validated with a larger patient population.

Figure 7 illustrates the boxplots of the five features that were utilized to classify the two patients whose ovaries were imaged both *in vivo* and *ex vivo*. Comparison of the *ex vivo* and *in vivo* data shows similarity in terms of the range of the selected features. By utilizing the *ex vivo* data-trained logistic classifier for the *in vivo* PAT/US image frames, 12 out of 14 malignant image frames (86% sensitivity) and all 17 benign image frames (100% specificity) were accurately classified. Again, by using the *ex vivo* data-trained SVM classifier for the *in vivo* PAT/US imaging frames, 10 out of 14 malignant imaging frames (71% sensitivity) and all 17 benign imaging frames (100% specificity) were correctly classified. Interestingly, by using the *ex vivo* data-trained logistic classifier, which excluded image frames from the low-grade endometrioid carcinoma, the logistic classifier identified

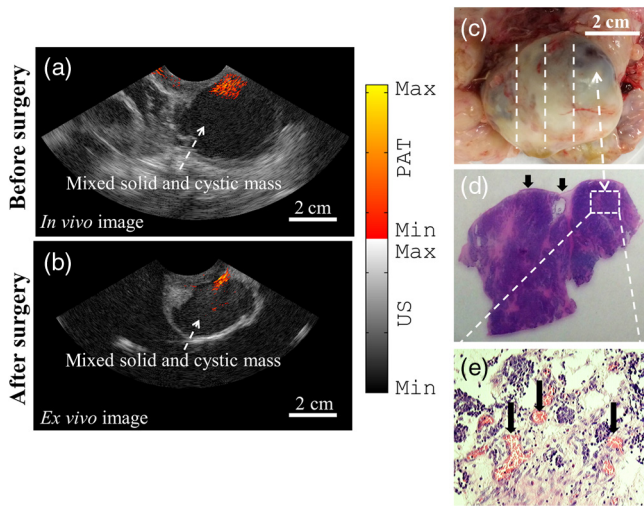


Fig. 4 (a) *In vivo* coregistered PAT/US image of a postmenopausal ovarian mass, (b) *ex vivo* coregistered PAT/US image of the same ovary after oophorectomy, and (c) photograph of the ovary. The dashed lines illustrate the 2-D PAT/US scan positions and the corresponding H&E cuts. (d) H&E staining of the malignant area. The arrows point to the ovary surface. (e) Microvessels from the rectangular region indicated in (d).

13 out of 14 malignant imaging frames (94% sensitivity), and one benign image frame was also identified as carcinoma. All 17 benign image frames were identified as benign (94% specificity). The SVM diagnostic performance did not change. Again,

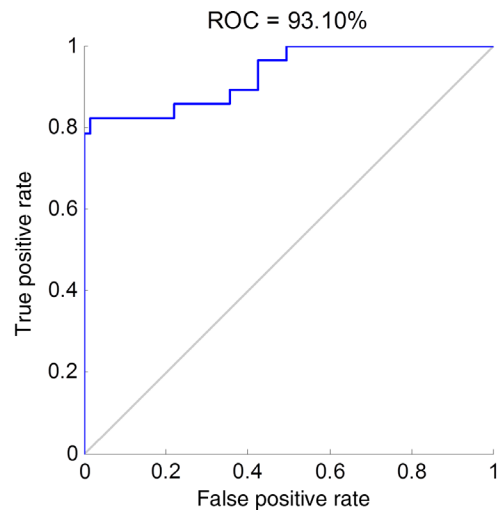


Fig. 6 An example of ROC curve of one testing data.

no conclusion can be drawn due to the limited *in vivo* data, and more patient data are needed to validate the result.

4 Discussion

In our previous *ex vivo* data classification study, we showed that SVM is slightly better than logistic classifier. This is also true for this new *ex vivo* data set. However, for the *in vivo* data reported in this study, the logistic classifier showed better performance than the SVM. Logistic regression is widely used in clinical

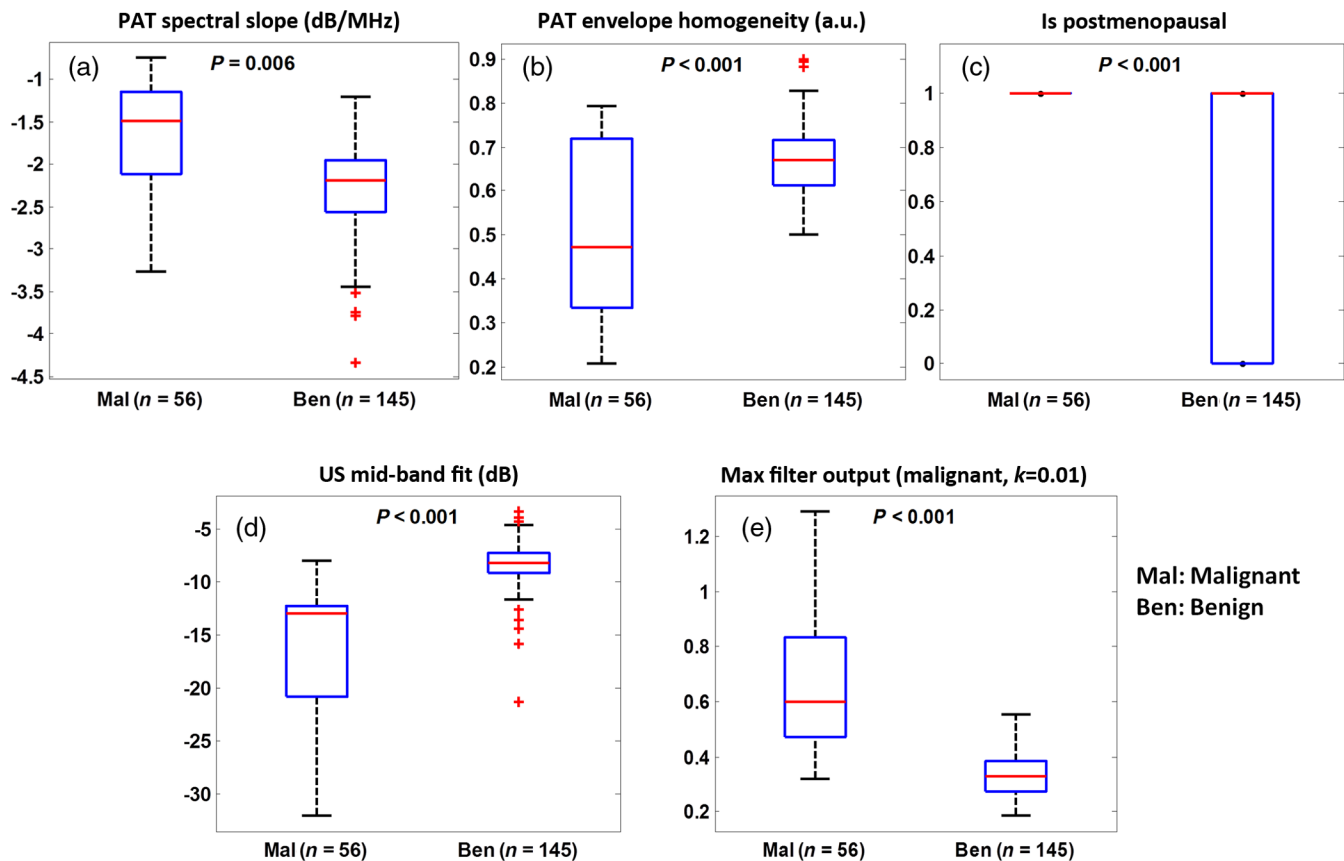


Fig. 5 Boxplots of *ex vivo* features: (a) PAT spectral slope; (b) PAT envelope homogeneity; (c) postmenopausal status (1 represents postmenopausal and 0 represents premenopausal); (d) US mid-band fit; and (e) malignant spatial filter output (malignant, $k = 0.01$).

Table 3 Sensitivity, specificity, PPV, and NPV of the logistic and SVM classifiers using five features.

Classifier	Sensitivity (%)		Specificity (%)		PPV (%)		NPV (%)	
	Training	Testing	Training	Testing	Training	Testing	Training	Testing
(a) Using all patients' data								
Logistic	85.64 ± 4.53	70.42 ± 6.29	87.14 ± 5.54	95.61 ± 3.17	87.06 ± 5.23	86.69 ± 7.46	85.86 ± 4.42	89.43 ± 2.01
SVM	99.57 ± 1.17	87.78 ± 4.32	99.27 ± 1.13	97.90 ± 1.59	98.24 ± 2.66	94.40 ± 3.90	99.83 ± 0.45	95.43 ± 1.53
(b) Excluding patient #4 with low-grade carcinoma								
Logistic	85.76 ± 4.64	82.08 ± 6.59	88.21 ± 4.42	92.85 ± 4.54	87.87 ± 4.36	82.74 ± 8.82	85.35 ± 4.12	93.20 ± 2.19
SVM	98.17 ± 1.02	90.53 ± 4.24	98.83 ± 1.23	96.91 ± 1.76	96.19 ± 3.96	92.16 ± 3.88	99.27 ± 0.56	96.41 ± 1.53

studies and has a smoother transition curve from the benign to malignant region. It can also provide an ROC curve and AUC, which are not available in SVM. SVM also has its own advantages. Since it only relies on support vectors, redundancy in the input data may not affect its performance. Thus, we have included both classifiers and further studies with more *in vivo* data will provide a more definitive answer on which classifier is better for *in vivo* classification of patient data.

The mapping between PAT beam envelopes above the system noise threshold and PAT images is a linear relationship. However, each image is normalized to its own maximum,

which varies from frame to frame, while each beam envelope varies according to the light fluence and tissue absorption along the angular path. To examine the effect of potential correlation of PAT beam envelope homogeneity and max malignant spatial filter output from PAT images on both classifiers, we have computed the Pearson's correlation coefficient r of these two features and found a weak correlation of $r = 0.25$. When both max malignant spatial filter and PAT envelope homogeneity were used together with the remaining three optimal features (PAT spectral slope, US mid-band fit, and menopausal status), the classifiers provided improved performance than

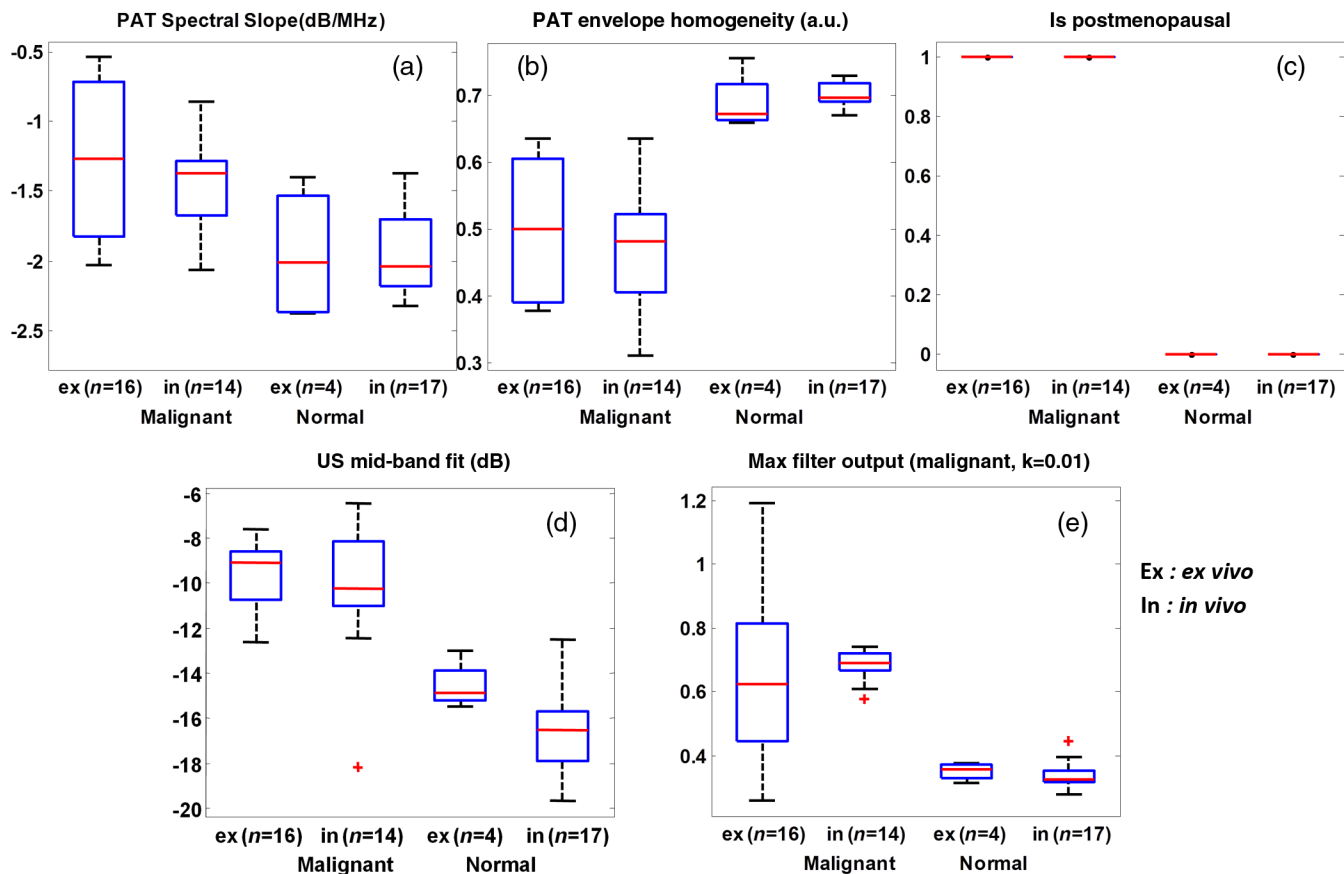


Fig. 7 Boxplots for two *in vivo* patient studies: (a) PAT spectral slope; (b) PAT envelope homogeneity; (c) postmenopausal status; (d) US mid-band fit; and (e) malignant spatial filter output (malignant, $k = 0.01$).

that without max malignant spatial filter. Since the objective of optimal feature selection is to improve classification, we have kept the final five optimal features in the analysis.

This study has limitations. First, the *in vivo* patient data are limited due to difficulties in enrolling patients. However, the initial results using selected features obtained from *ex vivo* data to classify *in vivo* patients' ovarian masses are extremely encouraging. Future efforts will be focused on patient enrollment and validation of the initial results reported in this study. Second, 5 to 10 imaging frames obtained at different locations of the same ovary were used as independent images for the classifier input. We have minimized the use of correlated images by selecting visually different images from a sequence of images obtained from the same ovary and performed 50 times cross-validation. Thus, the effect of some correlation of inputs on classifier performance is minimized, especially on the performance of the nonlinear SVM classifier. Third, multiple wavelengths data were acquired from *in vivo* patients in an effort to extract oxygen saturation of the ovarian mass for improving diagnosis based on absorption only. However, because features were extracted from excised ovaries, oxygen saturation is not meaningful in characterizing these ovaries. Future efforts will also be focused on extracting wavelength-dependent features for improving the ovarian tissue classification.

5 Summary

In this study, *ex vivo* ovarian tissues with malignant and benign diagnosis were imaged using our optimized coregistered PAT/US system, and quantitative analysis was performed by extracting features from PAT and US data. By utilizing a five-feature logistic model and SVM to classify the benign and malignant *ex vivo* ovary images, a sensitivity of 70.4% and specificity of 95.6% were achieved using the logistic model, whereas a sensitivity of 87.7% and specificity of 97.9% were obtained from SVM, in the testing sets. Furthermore, two patients with benign and malignant ovarian masses were non-invasively imaged before oophorectomy. The logistic classifier accurately identified 12 out of 14 imaging frames from a high-grade, early-stage serous epithelial carcinoma (86% sensitivity), and all 17 images from a benign ovarian mass (100% specificity). The SVM correctly identified 10 out of 14 imaging frames obtained from the malignant mass (71% sensitivity) and all 17 imaging frames from the benign mass (100% specificity). These initial results demonstrate that the PAT/US system and image classifier algorithm are capable of *in vivo* imaging of vascular distributions in ovarian tissue and accurate classification. Future efforts will be focused on overcoming enrollment challenges and further validation of these promising initial results.

Recently, a large-scale systematic review and meta-analysis was performed, and it was concluded that screening asymptomatic women for ovarian cancer does not reduce mortality or diagnosis at an advanced stage and is associated with unnecessary surgery.⁷ Our data from 15 symptomatic patients who were undergoing PO have shown that one patient had an early-stage T1c ovarian cancer. This was an accidental finding because this patient had enlarged ovarian mass seen by x-ray CT and transvaginal US. However, our results using PAT/US feature analysis have shown that 12 out of 14 imaging frames from this high-grade, early-stage epithelial carcinoma (86% sensitivity) can be correctly identified. This is an encouraging result and will need to be validated from a larger patient population.

Appendix

The spatial filter output is given by the following 2-D form:²⁵

$$H^*(\mu, \nu) = \frac{E[S(\mu, \nu, x_0, y_0)e^{j(x_0\mu + y_0\nu)}]}{E[|S(\mu, \nu, x_0, y_0)|^2]}, \quad (1)$$

where $H^*(\mu, \nu)$ is the complex conjugate of the 2-D frequency response of the filter with μ and ν denoting the spatial frequencies; the expectation E is taken from PAT image $S(\mu, \nu, x_0, y_0)$ at different (x_0, y_0) within the selected ROI. Nonlinear filters have some additional nonlinear operators to be applied to the amplitude of image frequency spectrum.

$$S'(\mu, \nu) = |S(\mu, \nu)|^k e^{i\phi_s(\mu, \nu)}, \quad (2)$$

where S' is the nonlinearized version of S and its phase ϕ_s is unmodified while amplitude is powered to order parameter k ($0 < k < 1$). The linear version ($k = 1$) gives the best recognition SNR if the image has only white noise.²⁶ Study shows that the use of nonlinearities in the Fourier plane of pattern recognition correlators can improve correlator performance and make it more tolerant to distortion,³⁶ such as scaling and rotation. Additional nonlinear versions were achieved by setting k to 1/3 (cubic root) and 0.01 (binary). Both of them have better SNR than the linear one in case the image has colored noise.²⁶ The spatial filters constructed from PAT malignant and benign training images act as the malignant template and the benign template. For any incoming PAT image, a high output from the malignant template and a low output from the benign template are classified as a malignant case. Similarly, a PAT image is classified as a benign case if the output from the malignant filter is low while the output from the benign filter is high. For the definition of other features, readers can refer to Refs. 20 and 21 for more details.

Acknowledgments

This research was supported by the National Cancer Institute (NIH R01CA151570). The authors would like to thank Karen Metersky for consenting patients and Melissa Parente for coordinating the tissue specimen study.

References

1. C. N. Landen, Jr., M. J. Birrer, and A. K. Sood, "Early events in the pathogenesis of epithelial ovarian cancer," *J. Clin. Oncol.* **26**(6), 995–1005 (2008).
2. D. L. Clarke-Pearson, "Screening for ovarian cancer," *N. Engl. J. Med.* **361**, 170–177 (2009).
3. M. A. Brewer et al., "Imaging of the ovary," *Technol. Cancer Res. Treat.* **3**(6), 617–627 (2004).
4. S. M. Domchek, J. E. Stopfer, and T. R. Rebbeck, "Bilateral risk-reducing oophorectomy in BRCA1 and BRCA2 mutation carriers," *J. Natl. Compr. Canc. Netw.* **4**(2), 177–182 (2006).
5. S. M. Domchek and T. R. Rebbeck, "Prophylactic oophorectomy in women at increased cancer risk," *Curr. Opin. Obstet. Gynecol.* **19**(1), 27–30 (2007).
6. C. Marchetti et al., "Hormone therapy in oophorectomized BRCA1/2 mutation carriers," *Menopause* **21**(7), 763–768 (2014).
7. C. J. Reade et al., "Risks and benefits of screening asymptomatic women for ovarian cancer: a systematic review and meta-analysis," *Gynecol. Oncol.* **130**(3), 674–681 (2013).
8. C. Bodelon et al., "Analysis of serial ovarian volume measurements and incidence of ovarian cancer: implications for pathogenesis," *J. Natl. Cancer Inst.* **106**(10), dju262 (2014).

9. L. V. Wang and S. Hu, "Photoacoustic tomography: in vivo imaging from organelles to organs," *Science* **335**(6075), 1458–1462 (2012).
10. S. Sethuraman et al., "Spectroscopic intravascular photoacoustic imaging to differentiate atherosclerotic plaques," *Opt. Express* **16**(5), 3362–3367 (2008).
11. S. A. Ermilov et al., "Laser optoacoustic imaging system for detection of breast cancer," *J. Biomed. Opt.* **14**(2), 024007 (2009).
12. J. Gamelin et al., "Curved array photoacoustic tomographic system for small animal imaging," *J. Biomed. Opt.* **13**(2), 024007 (2008).
13. A. Karabutov et al., "Backward mode detection of laser-induced wide-band ultrasonic transients with optoacoustic transducer," *J. Appl. Phys.* **87**, 2003–2014 (2000).
14. A. Aguirre et al., "Potential role of coregistered photoacoustic and ultrasound imaging in ovarian cancer detection and characterization," *Trans. Oncol.* **4**(1), 29–37 (2011).
15. R. A. Kruger et al., "Thermoacoustic computed tomography using a conventional linear transducer array," *Med. Phys.* **30**(5), 856–860 (2003).
16. P. D. Kumavor et al., "Co-registered pulse-echo/photoacoustic transvaginal probe for real time imaging of ovarian tissue," *J. Biophotonics* **6**(6–7), 475–484 (2013).
17. U. Alqasemi et al., "Interlaced photoacoustic and ultrasound imaging system with real-time coregistration for ovarian tissue characterization," *J. Biomed. Opt.* **19**(7), 076020 (2014).
18. H. S. Salehi et al., "Design of optimal light delivery system for co-registered transvaginal ultrasound and photoacoustic imaging of ovarian tissue," *Photoacoustics* **3**(3), 114–122 (2015).
19. H. S. Salehi et al., "Design of miniaturized illumination for transvaginal co-registered photoacoustic and ultrasound imaging," *Biomed. Opt. Express* **5**(9), 3074–3079 (2014).
20. U. Alqasemi et al., "Recognition algorithm for assisting ovarian cancer diagnosis from coregistered ultrasound and photoacoustic images," *J. Biomed. Opt.* **17**(12), 126003 (2012).
21. H. Li et al., "Utilizing spatial and spectral features of photoacoustic imaging for ovarian cancer detection and diagnosis," *J. Biomed. Opt.* **20**(1), 016002 (2015).
22. *American National Standard for the Safe Use of Lasers ANSI Z136*, pp. 1–2007, Laser Institute of America, Orlando, Florida (2007).
23. G. Xu et al., "The functional pitch of an organ: quantification of tissue texture with photoacoustic spectrum analysis," *Radiology* **271**(1), 248–254 (2014).
24. T. Wang et al., "Characterization of ovarian tissue based on quantitative analysis of photoacoustic microscopy images," *Biomed. Opt. Express* **4**(12), 2763–2768 (2013).
25. A. Javidi and J. Wang, "Optimum distortion-invariant filter for detecting a noisy distorted target in nonoverlapping background noise," *J. OSA* **12**(12), 2604–2614 (1995).
26. N. Towghi, L. Pan, and B. Javidi, "Noise robustness of nonlinear filters for image recognition," *J. Opt. Soc. Am. A* **18**(9), 2054–2071 (2001).
27. F. L. Lizzi et al., "On the statistics of ultrasonic spectral parameters," *Ultrasound Med. Biol.* **32**(11), 1671–1685 (2006).
28. A. J. Feleppa et al., "Diagnostic spectrum analysis in ophthalmology: a physical perspective," *Ultrasound Med. Biol.* **12**, 623–631 (1986).
29. J. Feleppa et al., "Ultrasonic spectrum-analysis and neural-network classification as a basis for ultrasonic imaging to target brachytherapy of prostate cancer," *Brachytherapy* **1**, 48–53 (2002).
30. S. K. Alam et al., "Computer aided diagnosis of breast lesions using a multifeature analysis procedure," *SPIE Med. Imaging* **4687**, 296–303 (2002).
31. D. Timmerman et al., "Logistic regression model to distinguish between the benign and malignant adnexal mass before surgery: a multicenter study by the International Ovarian Tumor Analysis Group," *J. Clin. Oncol.* **23**(34), 8794–8801 (2005).
32. N. Dikaos et al., "Logistic regression model for diagnosis of transition zone prostate cancer on multi-parametric MRI," *Eur. Radiol.* **25**(2), 523–532 (2015).
33. D. Kleinbaum et al., *Applied Regression Analysis and Other Multivariable Methods*, 3rd ed., Duxbury Press, (1998).
34. N. Cristianini and J. Shawe-Taylor, *An Introduction to Support Vector Machines and Other Kernel-Based Learning Methods*, Cambridge University Press, Cambridge, England (2000).
35. M. Kudo and J. Sklansky, "Comparison of algorithms that select features for pattern classifiers," *Pattern Recognit.* **33**(1), 25–41 (2000).
36. A. Javidi and D. Painchaud, "Distortion-invariant pattern recognition with Fourier-plane nonlinear filters," *Appl. Opt.* **35**(2), 318–331 (1996).

Biographies for the authors are not available.